



Delft University of Technology

## Fracture-Induced Permeability in Whitby Mudstone

Houben, Maartje E.; van Eeden, Jasmijn C.M.; Barnhoorn, Auke; Hangx, Suzanne J.T.

**DOI**

[10.1021/acs.est.0c00557](https://doi.org/10.1021/acs.est.0c00557)

**Publication date**

2020

**Document Version**

Final published version

**Published in**

Environmental science & technology

**Citation (APA)**

Houben, M. E., van Eeden, J. C. M., Barnhoorn, A., & Hangx, S. J. T. (2020). Fracture-Induced Permeability in Whitby Mudstone. *Environmental science & technology*, 54(15), 9564-9572.  
<https://doi.org/10.1021/acs.est.0c00557>

**Important note**

To cite this publication, please use the final published version (if applicable).  
Please check the document version above.

**Copyright**

Other than for strictly personal use, it is not permitted to download, forward or distribute the text or part of it, without the consent of the author(s) and/or copyright holder(s), unless the work is under an open content license such as Creative Commons.

**Takedown policy**

Please contact us and provide details if you believe this document breaches copyrights.  
We will remove access to the work immediately and investigate your claim.

# Fracture-Induced Permeability in Whitby Mudstone

Maartje E. Houben, Jasmijn C. M. van Eeden, Auke Barnhoorn, and Suzanne J. T. Hangx\*



Cite This: *Environ. Sci. Technol.* 2020, 54, 9564–9572



Read Online

ACCESS |



Metrics & More



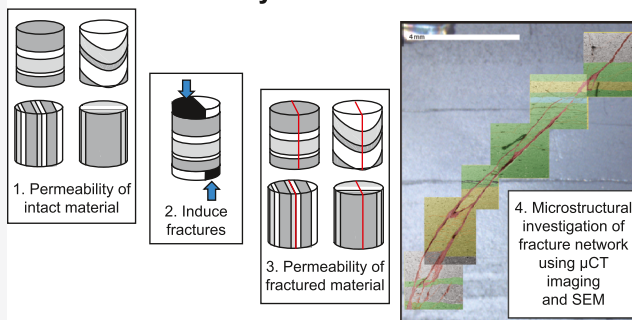
Article Recommendations



Supporting Information

**ABSTRACT:** Shale host rock and containment potential are largely determined by the connected pore network in the rock, and the connection between the pore network and the naturally present or mechanically induced fracture network together determines the total bulk permeability. Pore connectivity in shales is poorly understood because most of the porosity is present in sub-micrometer-sized pores that are connected through nanometer-sized pore throats. We have used a number of different techniques to investigate the microstructure and permeability of Early Jurassic shales from the UK (Whitby Mudstone), under intact and fractured conditions. Whitby Mudstone is a clay matrix-rich rock (50–70%), with different mineralogical layers on the sub-millimeter scale and very low natural permeability ( $10^{-19}$  to  $10^{-22}$  m<sup>2</sup>), representative of many gas shales and caprocks present in Europe. Artificial fracturing of this shale increases its permeability by 2–5 orders of magnitude at low confining pressure (5 MPa). At high confining pressures (30 MPa), permeability changes were more sensitive to the measuring direction with respect to the bedding orientation. Given the distinct lack of well-defined damage zones, most of the permeability increase is controlled by fracture permeability, which is sensitive to the coupled hydro-chemo-mechanical response of the fractures to fluids.

## Workflow for Whitby Mudstone



## 1. INTRODUCTION

Shales and mudstones are of major interest as potential host formations for radioactive waste disposal and as sealing horizons for CO<sub>2</sub> storage.<sup>1–3</sup> Understanding possible fluid pathways in shales is a critical step toward assessing the potential risks for fluid leakage along (pre-existing) faults or fractures.<sup>4–7</sup> Furthermore, shales are unconventional reservoirs for natural gas,<sup>8</sup> and understanding fluid pathways helps to predict their reservoir potential. Fluid flow in the context of containment integrity and gas shale production is largely determined by the connected pore network present in the intact rock, and the connection between this pore network and the pre-existing, or induced, fracture network.<sup>9–13</sup> Pore connectivity in shales is poorly understood because most of the porosity is present in the form of sub-micrometer-sized pores that are connected through nanometer-sized pore throats,<sup>14–21</sup> making them difficult to study. Faults in shales are known to act as seals, and they form more permeable fluid pathways in reservoirs.<sup>12,22–24</sup> In general, faults consist of a fine-grained low-permeable core surrounded by a permeable damage zone.<sup>25–28</sup> In shale-rich formations, fault zones tend to have a thin fault core and damage zone, leading to a narrow fault zone width.<sup>25</sup> However, the complex microstructure of shales and fast weathering of shale faults in outcrop<sup>29</sup> makes that fluid flow through fractured shales is still poorly understood.<sup>12,22</sup>

Induced faults and fractures alter the physical structure of reservoirs and cap rocks, thereby changing the (local) transport properties.<sup>13,30</sup> However, the geometry of the fracture network will depend on the orientation of the stress regime with respect to the bedding or could be related to strain localization around heterogeneities in the microstructure.<sup>31</sup> To assess fracture network geometry and the influence of bedding orientation thereon, and permeability changes due to fracture network development, we performed direct shear experiments to induce fractures, for varying bedding geometries, and measured bulk (gas) permeability pre- and post-deformation, as a function of mean stress. We used the clay-rich Whitby Mudstone, an analogue for many caprocks, source rocks, and shale gas plays in Europe comparable to the Posidonia Shale.<sup>32</sup> Whitby Mudstone is a clay-rich rock (50–70% clay matrix, mainly illite<sup>20</sup>), with distinct mineralogical layering on the sub-millimeter scale, an average TOC content of about 4%, and very low natural matrix permeability ( $10^{-19}$  to  $10^{-22}$  m<sup>2</sup>).<sup>33</sup> The fracture network was imaged using X-ray microtomography and scanning electron microscopy (SEM).

Received: January 28, 2020

Revised: July 2, 2020

Accepted: July 6, 2020

Published: July 6, 2020



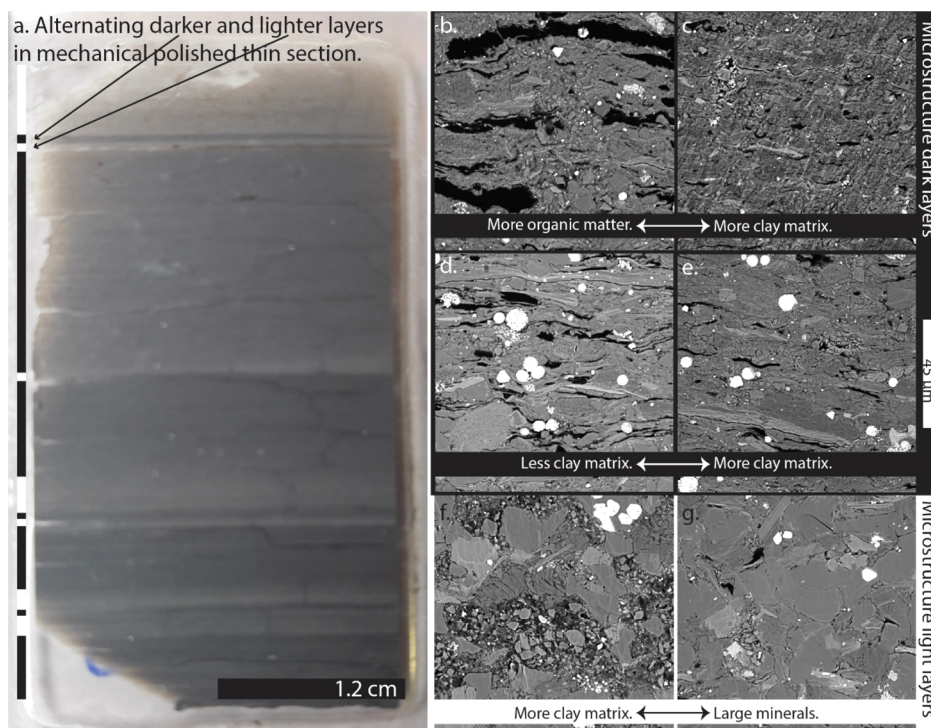


**Figure 1.** Microstructure Whitby Mudstone of the undeformed sample. (a) Thin section overview showing clearly the alternating darker and lighter layers. (b–g) Higher magnification microstructures of the different layers present in the thin section. Differences in clay matrix amount, organic matter amount, and amount of silt-sized grains define the different microstructures encountered.

## 2. MATERIALS AND METHODS

**2.1. Sample Material.** All samples originated from the same layer of Whitby Mudstone (UK) and were collected from the wave cut platform located circa 3 m below the Whalestones, striving for a homogeneous mineralogy between different samples.<sup>20,34,35</sup> The samples were transported and stored in sealed containers filled with local sea water to avoid drying. Five cores were prepared for this study with a 25 mm diameter (30–43 mm length), with different bedding orientations: bedding-perpendicular (WMF500A,  $\perp$ ), bedding-parallel (WMF500C/-D/-E,  $\parallel$ ), and oblique to bedding ( $65^\circ$  angle, WMF500B,  $\searrow$ ). Immediately after wet-coring of the samples, the samples were sleeved in fluorinated ethylene propylene (FEP) to avoid drying-induced breakage. The samples were left to dry in an oven at  $50^\circ\text{C}$  for about a week prior to the experiments.

**2.2. Experimental Approach.** Permeability measurements were performed to assess the bulk permeability of the intact and fractured material, respectively. The transient step method was employed, using argon gas as the pore fluid<sup>36–38</sup> to avoid swelling effects often observed when using other fluids such as water or  $\text{CO}_2$ .<sup>39–42</sup> The lowest measurable permeability using the argon permeameter (see the Supporting Information, S1.1) is approximately  $\sim 10^{-22}$  m<sup>2</sup>, limiting permeability measurements on lower permeable samples.<sup>36,43</sup> After determination of the intact shale permeability, the samples were deformed in direct shear<sup>12</sup> to create a fracture network. All deformation experiments were performed dry, at room temperature, at a confining pressure of 30 MPa, and an axial strain rate of  $\sim 10^{-5}$  s<sup>-1</sup>. Load was increased until failure occurred, as indicated by a loss of differential stress across the sample (see the Supporting Information, S1.2). Subsequently, the permeability of the fractured samples was measured. Note that sample WMF500E

was not deformed but manually split along its axis using a sharp knife, simulating a tensile fracture.

**2.3. Image Analyses.** We used X-ray micro-tomography imaging to visualize the fracture network (20–25  $\mu\text{m}$  voxel resolution<sup>12,44–49</sup>). Fractures with a sufficiently wide aperture ( $\gg 20\text{--}25\ \mu\text{m}$ ) were filtered out using a simple threshold method, while narrower fractures were segmented manually. To obtain detailed images of the fracture network, at higher resolutions than the computed tomography (CT) images, the samples were impregnated with Araldite2020 epoxy resin and cut in half lengthwise. One half of the sample was mechanically polished and used to prepare thin sections. The other half was used to prepare broad-ion-beam (BIB)-polished sections out of selected areas of the fracture system (Precision Ion Polishing System; Fischione, model 1060). For comparison, undeformed Whitby Mudstone formation (WMF) material of the same block was also sectioned. Visual inspection of pre- and postexperiment material was performed using a scanning electron microscope (JEOL Neoscope II JCM-6000, FEI HELIOS nanolab DualBeam 3G). Both secondary electron (SE) and backscatter electron (BSE) modes were used to image fractures, mineralogy, and porosity.<sup>20,33</sup> Details of all methods can be found in the Supporting Information Section S1.

## 3. RESULTS

**3.1. Intact Whitby Mudstone.** The intact material is characterized by a clear alternation of darker and lighter layers, easily recognized in thin section (Figure 1a). The darker layers are richer in organic matter and clay matrix, while the lighter layers are more quartz- and carbonate-rich and show a coarser average grain size (cf. Figure 1b–e vs f,g). It should be noted



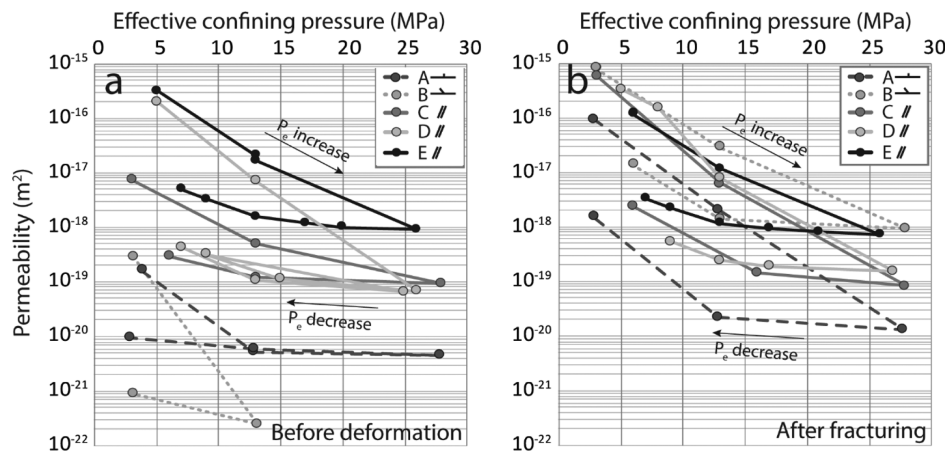


**Figure 2.** Permeability data vs. effective confining pressure for samples A to E. (a) Intact samples. (b) Fractured samples.

that fractures roughly following the bedding orientation are visible in all samples even prior to active fracturing.

Argon gas permeability of intact WMF was measured at effective confining pressures  $P_e$  of 3–28 MPa ( $P_e$  is equal to the applied confining pressure,  $P_c$ , minus pore pressure,  $P_p$ ), as shown in Figure 2a. When increasing  $P_e$  from 3 to 28 MPa, sample permeability decreased by 2–4 orders of magnitude (from  $2 \times 10^{-16}$  to  $3 \times 10^{-19}$  m<sup>2</sup> at low  $P_e$ , to  $9 \times 10^{-19}$  to  $3 \times 10^{-22}$  m<sup>2</sup> at high  $P_e$ ). Upon decreasing confinement, permeability increased again, although it never reached the initial permeability values. This  $P_e$ – $\kappa$  behavior was maintained upon subsequent confinement cycling (see sample WMF500D in Figure 2a). Samples with gas flow parallel to bedding had the highest permeability, despite an approximately 1 order of magnitude variation in permeability between samples with the same bedding orientation (cf. WMF500C/D/E, Figure 2a). At high confining pressures ( $P_e = 28$  MPa), bedding-parallel samples showed permeability values between  $9 \times 10^{-19}$  and  $9 \times 10^{-20}$  m<sup>2</sup>, while bedding-perpendicular permeability was measured to be an order of magnitude lower ( $\kappa = 5 \times 10^{-21}$  m<sup>2</sup>). For the bedding-oblique sample, permeability was too low to measure at  $P_e$  of more than 13 MPa (i.e.,  $<10^{-22}$  m<sup>2</sup>, Figure 2a).

**3.2. Fractured Whitby Mudstone.** Samples WMF500A–D were deformed in direct shear to generate a shear fracture network (Supporting Information S1.2). Peak differential stress upon failure ranged from 40 to 55 MPa for all four samples (Figure S4), with samples WMF500B and -C being the weakest and -D being the strongest. Upon loading, all samples showed a near-linear increase in differential stress with increasing axial strain. Following peak stress, displacement was continued to shear strains of 1.2–3.4% (i.e., 0.5–1.5 mm displacement). Shear-fractured sample permeability values showed similar trends to those measured for the intact material (cf. Figure 2a,b). The initial permeability (at  $P_e = 5$  MPa) for the fractured cores (WMF500A–D) was higher after deformation, but as soon as the core had experienced an effective pressure of almost 30 MPa, the permeability after fracturing was similar to the permeability before fracturing (WMF500A  $\perp$ , C  $\parallel$ , and D  $\parallel$ ). Permeability values measured after the maximum  $P_e$  had been reached did not go back to the initial permeability values both before and after fracturing. In terms of the effect of bedding orientation, the largest increase in permeability was observed for the bedding-oblique sample (WMF500B,  $\searrow$ ) both at low and high  $P_e$ , displaying a 3–5

orders of magnitude permeability increase (from  $3 \times 10^{-19}$  to  $3 \times 10^{-22}$  to  $9 \times 10^{-16}$  to  $1 \times 10^{-18}$  m<sup>2</sup>). For the bedding-perpendicular sample (WMF500A,  $\perp$ ), fracturing also increased permeability, but only up to 3 orders of magnitude at low  $P_e$  (from  $2 \times 10^{-19}$  –  $5 \times 10^{-21}$  to  $1 \times 10^{-16}$  –  $2 \times 10^{-20}$  m<sup>2</sup>). For fractured, bedding-parallel material, permeability was the least affected (WMF500C/-D;  $\parallel$ ), displaying only a factor of 1 to 3 increase in permeability (from  $2 \times 10^{-16}$  –  $7 \times 10^{-20}$  to  $6 \times 10^{-16}$  –  $9 \times 10^{-20}$  m<sup>2</sup>). Note that the bedding-parallel samples WMF500C and D were deformed in direct shear at parallel and perpendicular directions to the shear plane, respectively. After deformation, WMF500C showed an overall slight increase in permeability, whereas WMF500D only showed a permeability increase at low  $P_e$  (3–15 MPa) and a similar permeability at high  $P_e$  (28 MPa; Supporting Information, S2.1) compared to the initial, intact permeability at the same  $P_e$ . Note that for the split (tensile fractured) sample WMF500E ( $\parallel$ ), permeability after fracturing was very similar overall and even marginally lower than for the intact material under all  $P_e$ -conditions (Table S1).

**3.3. CT-Imaging of the Fracture Network.** On the sample scale, visual inspection and CT imaging of the cores confirmed that deformation of samples WMF500A–D led to the development of shear fractures in all four cores. However, it appeared that on the core scale, not all large fractures were through-going from top to bottom, as observed for samples WMF500A, D. Typically, fractures emerge from the sample-piston contact, cross-cutting, and/or following the bedding orientation. All created shear fractures tend to rotate from the sample-piston contact toward the circumference of the core (Figure 3). The angle at which the bedding is cross-cut by the formed fractures changes with distance from the sample-piston contact. Furthermore, for cores WMF500D ( $\parallel$ ) and WMF500E ( $\parallel$ ), CT images were taken before and after fracturing (Figure 3d–h). For the samples deformed in direct shear (WMF500A–D), the fracture networks consist of an anastomosing fracture system containing several fracture branches (see Figure 3), while in addition, interactions between pre-existing drying fractures and newly induced fractures can be observed in samples WMF500D–E comparing the before and after CT images (see Figure 3). In line with the visual inspection, samples WMF500B ( $\searrow$ ) and WMF500C ( $\parallel$ ) showed the clear development of a fracture network throughout the entire core. In samples WMF500A ( $\perp$ ) and WMF500D ( $\parallel$ ) also, new fractures formed, but these did not



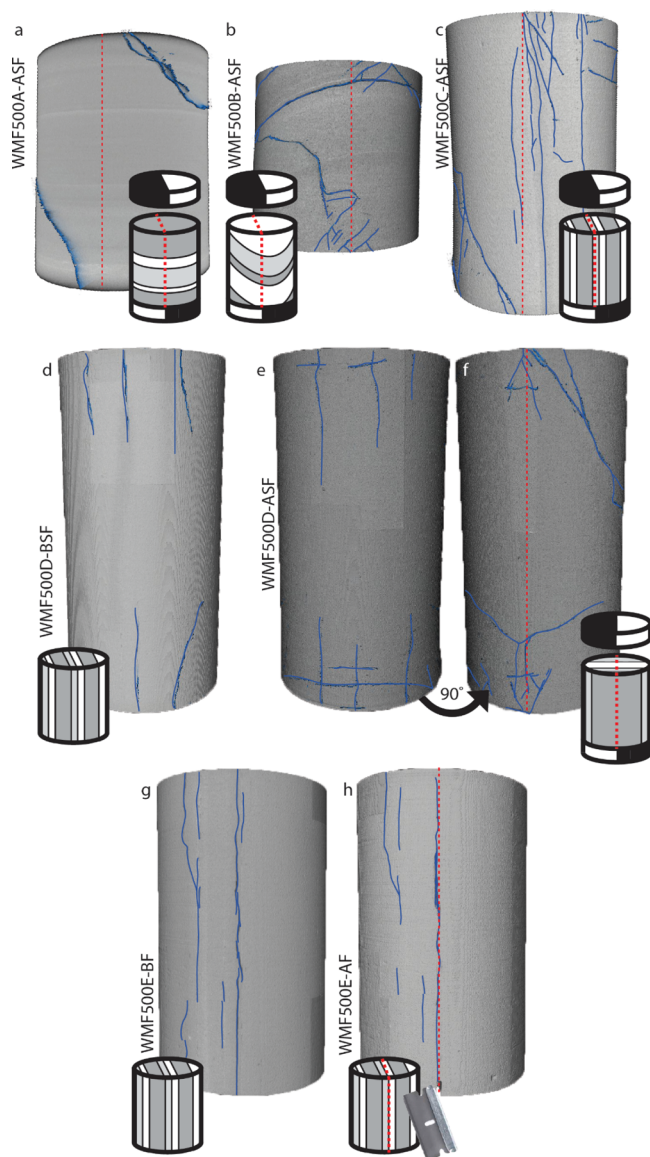


**Figure 3.** Volume rendering of the CT data for samples WMF500A to E, before (BF) and after shear (ASF) and manual (AF) fracturing. Note that the red dotted lines indicate roughly the orientation of the expected shear fracture, while the blue lines indicate the actual fractures observed in the samples before and after fracturing. (a–c) Cores WMF500A–C after fracturing. (d) Core WMF500D, showing pre-existing fractures present in the sample before deformation. (e,f) Core WMF500D after fracturing, where (e,f) are views of the core with a 90° angle in between. (g) Core WMF500E before splitting of the sample, displaying pre-existing fractures. (h) Core WMF500E after splitting of the sample.

extend throughout the entire sample, connecting top and bottom. It should be noted that for sample WMF500A, an increase in permeability was observed post-fracturing, despite the shear fractures not connecting both sample ends. For all CT images, it should be taken into account that given their 20–25  $\mu\text{m}$  resolution, it is likely that smaller cracks, contributing to the percolating network, are not visualized.

### 3.4. Detailed SEM Imaging of the Damage Zone.

Typically, a fracture damage zone is defined as a zone surrounding the main fracture(s), exhibiting grain size reduction, visible grain breakage, changes in clay mineral orientation, and/or an increase in crack density.<sup>50,51</sup> In general,

in the mechanically damaged Whitby Mudstone samples, observed fault zones within the samples are composed of multiple gouge-filled fractures up to tens of micrometers wide forming anastomosing patterns, where the transition from the damage zone to undisturbed host rock is mostly abrupt (Figure 4; Supporting Information, S3) except for layers with more silt-sized grains where a damage zone is present [e.g., Figure 4(a2)]. The main fractures are flanked by subsidiary, branching fractures, separated by slivers of relatively intact material [Figure 4(a3)]. In highly clay-rich zones, the fractures are narrow [up to 20  $\mu\text{m}$ ; Figure 4(a1,b4); Supporting Information, S3] to barely visible (Figure 4(a1,c7); Supporting Information, S3) with fracture widths up to several micrometers. Fractures localize in the fine-grained clay and organic matter-rich layers and mainly form around more competent grains, such as quartz and pyrite. When more competent larger minerals are present (e.g., quartz or carbonate) in the silt-sized layers, more damage is seen in the zones between different fractures, with obvious grain fracturing in larger grains [Figure 4(a2); Supporting Information, S3].

WMF500A ( $\perp$ ) shows an anastomosing fracture network that changes orientation and a damage zone width depending on the mineralogy of the layer (i.e., dark, organic matter/clay-rich vs. light, quartz- or carbonate-rich), with a higher angle of the fracture, with respect to the bedding, observed when fractures are entering a more competent (light) layer (Supporting Information, S3). Figure 4(a1) shows a narrow damage zone at the centre of the image (approx. 5  $\mu\text{m}$  wide) where a coarse- and fine-grained layer meet, whereas the damage zone broadens when two fine-grained or two coarse-grained layers meet. Figure 4(a2) displays a broader damage zone (>100  $\mu\text{m}$  wide) in a coarse-grained layer where the fracture core exists of fault gouge and broken up grains. Figure 4(a3) shows a broader (>50  $\mu\text{m}$  wide) damage zone in a fine-grained layer, where branching fractures are present. WMF500B ( $\searrow$ ) displays a fracture network of narrow fractures filled with fault gouge (Supporting Information, S3), where the mechanically induced fracture is a single fracture that interacts with bedding parallel fractures to form a fracture network connecting top and bottom of the sample. Figure 4(b4–b6) shows the fracture filled with gouge (20–100  $\mu\text{m}$  wide), where the border between the undamaged microstructure and the fracture is very abrupt showing a fault gouge-filled fracture. The damage zone in WMF500C ( $\parallel$ ) is broader than that in cores WMF500A ( $\perp$ ) and B ( $\searrow$ ), existing of lots of fractures mostly running semiparallel along the bedding (Supporting Information, S3; Figure 4c).

Shear displacement (up to tens of micrometers) along the main fractures is evidenced in samples WMF500A, B, and C by bending and breaking of phyllosilicates (Figure 5a,c–g), offsets seen in organic material particles (Figure 5b), breaking of mineral grains (Figure 5e), shearing of pyrite framboids (Figure 5f,h), and shear opening of fractures (Figures 4(b4–b6); 5b,f,h).

Overall, our experiments show most deformation (introduced fractures and surrounded damage zones) in the portion of the core driven by the stainless-steel semicylinder loading block (Figures 3, 4). The direct shear deformation experiments, coupled with CT imaging, show that the orientation of the bedding planes had a marked influence on fracture orientation, distribution, and extent. The shear fractured cores WMF500A–D showed 0.5–1.5 mm of displacement, and intended displacement along the fracture for core WMF500E

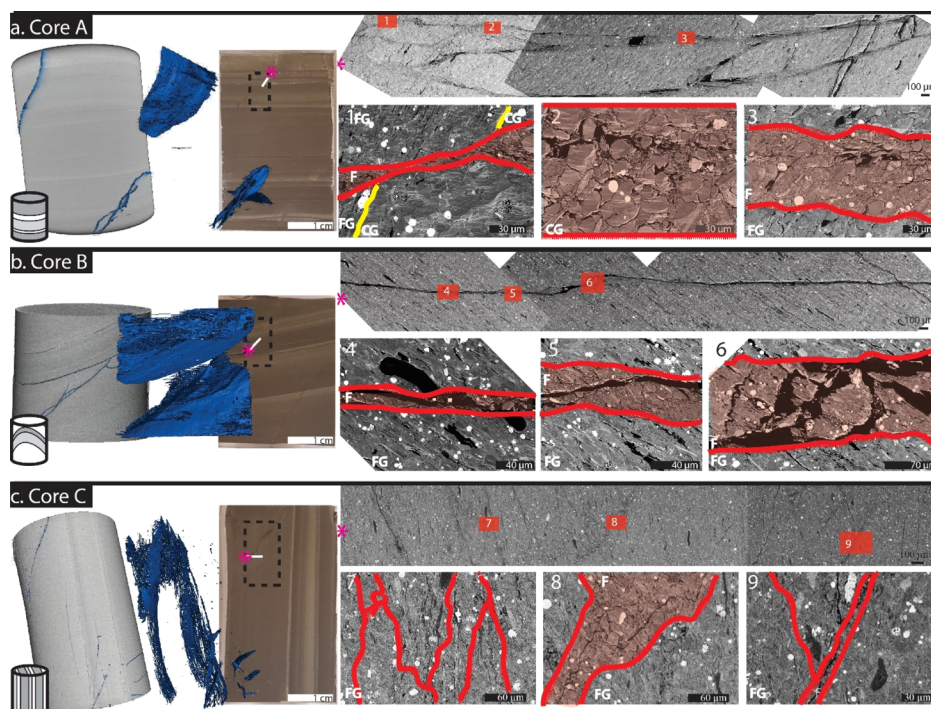


**Figure 4.** CT images of the fractured WMF500 cores (a) A, (b) B, and (c) C, together with an image of the thin sections and detailed SEM images of relevant sections of the fault zones. FG = fine-grained matrix; CG = coarse-grained matrix; F = fracture and damage zone; yellow line [a(A1)] indicating the border between two distinctly different bedding layers; red lines indicating a fracture; and damaged zones are indicated with a red see-through color. For more microstructural images of samples WMF500A, B, and C, please see the Supporting Information S3 Figures S5–S7.

was zero mm for this split cylinder crack. From the SEM images, the maximum displacement observed was about 60  $\mu\text{m}$ .

#### 4. DISCUSSION AND IMPLICATIONS

As shown by other studies as well,<sup>12,47,51</sup> fracture networks extending from one sample end to the other are more easily achieved in samples with the bedding parallel to the loading axis (conform sample WMF500C), with the bedding acting as a point of weakness<sup>52</sup> (Figures 3 and 4; Supporting Information S3). This is also seen in sample WMF500B, which shows a connected fracture network because of a fracture that formed partly along the bedding. As is typically observed for intact<sup>33,53,54</sup> and fractured<sup>12,46</sup> shales, permeability decreases with increasing effective confining pressures and permeability measured perpendicular to the bedding is lower than the permeability measured parallel to the bedding. For intact shale, this suggests that a better-connected pore/fracture pathway is present parallel to the bedding prior to deformation. Furthermore, as shown in our study, after fracturing of bedding-parallel material and after fracturing at an angle to the bedding, permeability measured at an angle to the bedding approaches the permeability measured parallel to the bedding. The largest permeability increase at high  $P_c$  was observed for sample WMF500B, which is assumed to be due to the formation of a fully connected fracture network throughout the whole of the core. This is in contrast to samples WMF500C and E (both bedding-parallel), which also showed fractures running from the top to the bottom of the cores but show hardly any change in permeability before and after fracturing at high  $P_c$ . This suggests that pre-existing bedding-parallel permeability in intact shales does not get significantly enhanced by the generation of bedding-parallel fractures, likely

as connectivity between higher permeability parts does not get enhanced much by fracturing. These results indicate that permeability along the bedding is in value very similar to the fracture permeability when the fractures are formed parallel to the bedding. This is in contrast to the effect fractures can be having when induced in bedding-oblique or -perpendicular cored material, as in those instances, induced fractures increased the permeability of the core at low and high  $P_c$ . By contrast, the core WMF500E (*II*, split) barely showed a permeability change before and after deformation, and permeability actually dropped slightly at all effective confinements, suggesting that we rather made the fracture surface smoother and/or the fracture aperture smaller by core-splitting and then mating of the cylinder halves.

Creep tests on quartz- and carbonate-rich shales (Haynesville, Barnett and Eagleford shale) demonstrated that more creep is obtained during compression of samples perpendicular to bedding, compared to parallel to the bedding.<sup>54</sup> Furthermore, these creep tests demonstrated that more clay- and organic matter-rich samples will display more creep.<sup>55,56</sup> As for most materials, creep of shales is suggested to follow a power-law function with time, although the amount of ductile creep and brittle strength of the material roughly scales with the elastic modulus of the rock. The clay- and organic matter-rich Whitby Mudstone has a Young's modulus of 8–20 MPa,<sup>57,58</sup> which means that the Whitby Mudstone falls in the highest creep compliance segment ( $>3 \times 10^{-5} \text{ MPa}^{-1}$ ),<sup>59</sup> compared to the more brittle Barnett, Haynesville, and Eagle Ford shales. The hysteretic behavior of our fractured shale samples could therefore be explained by permanent compaction of the cores during the first cycle of confining pressure increase.



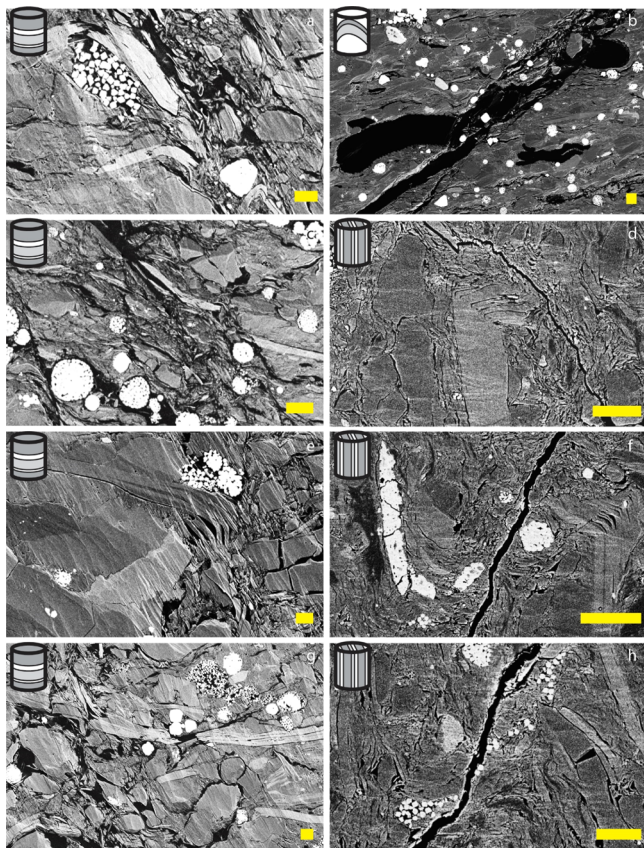


**Figure 5.** High-resolution SEM images of the fault zones in cores A, B, and C, where the scale bar = 5  $\mu\text{m}$ . (a) Shearing of phyllosilicate minerals into the damage zone; (b) breaking and offsetting of an organic material particle; (c) breaking of a phyllosilicate, part of the phyllosilicate is present in the damage zone, whereas the other part is present in the undamaged microstructure adjacent to the damage zone; (d) bending of a phyllosilicate into the damage zone; (e) bending and kinking of a phyllosilicate into the damage zone and breakage of some minerals; (f) bending and kinking into the damage zone of a phyllosilicate and an FeO mineral; (g) breakage and displacement of a phyllosilicate; and (h) shearing of pyrite framboids.

Whitby Mudstone is, because of its organic matter content (0–20%),<sup>34</sup> an unconventional source for hydrocarbon recovery. Mineralogically and microstructurally, the Whitby Mudstone is very similar to the Opalinus clay<sup>19,33,34</sup> that is a possible host rock for the storage of radioactive waste and CO<sub>2</sub>,<sup>1</sup> where the main difference between the two mudstones is the organic matter content. The type of fractures generated in our study are opening and shear fractures with very small displacements. They could represent fractures that form in an excavation damage zone surrounding a cavity used for radioactive waste storage. Although the fracture density and permeability close to the excavation is typically higher than what we measured in our experiments,<sup>60</sup> our experiments would represent the zone about 1 m away from the excavation. The results shown here imply that when dealing with a rock with >60% clay matrix, permeability of the excavation damaged zone about 1 m distance into the wall,<sup>1,60</sup> when the effective hydrostatic stress is >10 MPa (burial depth over 500 m deep), is very similar to the permeability of undamaged rock; hence, the deeper the radioactive waste repository, or the CO<sub>2</sub> sequestration site is buried, the less influence fractures have on the permeability increase of the host shale rock.

In the context of unconventional gas production, the fractures studied here could represent smaller fractures associated with hydraulic fracturing. Likewise, our results suggest that induced fracturing of an unconventional reservoir with the >60% clay matrix does not significantly increase rock permeability at  $P_e > 10$  MPa. At least, the small fractures generated will not significantly help to increase the permeability of the rock when the reservoir is buried deeper than about 500 m (burial depth of the Posidonia Shale in the Dutch subsurface is 1–3 km<sup>34</sup>), if they remain unpropped during the fracturing processes. In addition,  $P_e$  will increase over time in an unconventional reservoir because of the fact that upon extraction of the fluid from the pores/fractures, pore fluid pressure will drop, meaning that permeability will decrease over time during production with increasing  $P_e$ . It should be noted that the reduction in pore pressure may lead to desorption of water and gas from some of the clays, which could lead to shrinkage and the enhancement of permeability.<sup>42</sup>

The extraction of fluids (in the case of unconventional) or the injection of fluids (CO<sub>2</sub> storage) affects the permeability of the rock in general due to sorption-related processes impacting the matrix,<sup>42,61</sup> regardless of fractures being present or not. Extraction of fluid from the matrix affects the permeability of the rock by a change in the pressure gradient between the pore pressure and the overburden pressure and the swelling or shrinkage of the matrix.<sup>42</sup> On the other hand, the presence of water, whether in the liquid or vapor form, causes swelling of the matrix of Whitby Mudstone on the order of 0.6–2.2%.<sup>42</sup> Furthermore, studies<sup>61</sup> on Opalinus clay have shown that introducing CO<sub>2</sub> can cause swelling of shales, even at low swelling clay content (~5% for Opalinus clay), impacting fracture permeability, especially when the initial water activity of the clay is lower than the water activity of the injected CO<sub>2</sub>. In addition, introduction of CO<sub>2</sub> can cause chemical changes to the rock such as wettability alteration.<sup>56</sup> This interplay between hydraulic behavior, chemical interactions, and mechanical response to stress and swelling makes the production or leakage potential of fractured shales difficult to predict, especially since water saturation levels affect the Whitby Mudstone strength. The more water-saturated the Whitby Mudstone, the weaker it becomes, when strength of the rock is measured perpendicular to the bedding.<sup>62</sup> The work presented here shows that when no fluid rock interaction is assumed, the permeability of a dry shale with >60% clay matrix does not change significantly when the burial depth is >500 m. The fact that Whitby Mudstone weakens when water-saturated implies that we expect the permeability to change less under in situ conditions, since the rock will be saturated with fluids in the reservoir/repository.

Since in our experiments a substantial damage zone appears to be largely absent, that is, no identifiable fractures are visible outside the main fracture(s), it is possible to make a rough estimate of the permeability of the main fracture, assuming that the matrix permeability has not changed significantly. For this rough estimate, we assume that the main fracture can be simply represented by a parallel plate with a single aperture, allowing for laminar flow.<sup>63–67</sup> Note that the flow rate measured through a fractured core is a combination of the flow rate in the fracture and the flow rate in the matrix. For a simple fracture geometry, such as that displayed in sample WMF500A, this would mean that flow in the fractured portions of the sample is controlled by the fractures, while for the shortest



distance between the two fractures, the flow rate will be controlled by the undeformed matrix. Assuming that the fracture permeability ( $k_f$ ) can be approximated by  $k_f = \frac{w^2}{12}$ , through the hydraulic fracture aperture ( $w$ ),<sup>65</sup> then it is possible to make a rough prediction of the fracture permeability and fracture width. Accounting for the fracture angle, and hence the geometry of the shortest flow path between the top and the bottom of the sample, this means that under the highest confinement used in the experiments presented here (28 MPa), the fracture permeability is on the order of  $10^{-15}$  m<sup>2</sup>, with a hydraulic fracture aperture of several 100 nm. It should be taken into account that, given the assumptions on fracture geometry and flow paths, the predicted fracture apertures and fracture permeability are only rough estimates and should be rather viewed as order of magnitude estimates. Therefore, although fracture permeability is relatively high (6 orders of magnitude higher when compared to the undeformed matrix), the limited amount of fractured rock and the narrow fracture widths limit the permeability increase at the centimeter scale to 3 orders of magnitude. Logically, the deeper the rock is buried, the more fracturing-induced permeability changes depend on the extend, connectivity, and width of the fractures present in the produced fracture network, with shearing<sup>47</sup> potentially aiding in permeability enhancement.

## ■ ASSOCIATED CONTENT

### SI Supporting Information

The Supporting Information is available free of charge at <https://pubs.acs.org/doi/10.1021/acs.est.0c00557>.

Additional text on the experimental and analytical methods; more detailed descriptions of the results; seven supplementary figures, and one supplementary table (PDF)

## ■ AUTHOR INFORMATION

### Corresponding Author

Suzanne J. T. Hangx – Department of Earth Sciences, Utrecht University, 3585 CB Utrecht, The Netherlands;  
Email: [s.j.t.hangx@uu.nl](mailto:s.j.t.hangx@uu.nl)

### Authors

Maartje E. Houben – Department of Earth Sciences, Utrecht University, 3585 CB Utrecht, The Netherlands; [orcid.org/0000-0002-1687-7566](https://orcid.org/0000-0002-1687-7566)

Jasmijn C. M. van Eeden – Department of Earth Sciences, Utrecht University, 3585 CB Utrecht, The Netherlands

Auke Barnhoorn – Department of Geoscience and Engineering, Delft University of Technology, 2628 CN Delft, The Netherlands

Complete contact information is available at: <https://pubs.acs.org/doi/10.1021/acs.est.0c00557>

### Author Contributions

M.E.H. and S.J.T.H. conceived the project. The deformation experiments were performed by J.C.M.v.E. and S.J.T.H., while J.C.M.v.E. and M.E.H. performed the permeability measurements. A.B. performed the CT scans and their reconstruction. Image analysis (EM and CT) was done by M.E.H. The manuscript was written by M.E.H. and S.J.T.H., with

contributions of the other authors. All authors have given approval to the final version of the manuscript.

### Funding

M.E.H. was funded through a VENI grant from the Netherlands Organization for Scientific Research (NWO; 016.Veni.171.041).

### Notes

The authors declare no competing financial interest.

## ■ ACKNOWLEDGMENTS

We thank L. Hunfeld and R. Pijenburg with the preparation of the experiments. L. Bik is thanked for preparing the thin sections. F. van Oort and T. van der Gon Netscher are thanked for technical support in the mechanical experiments. A. Pluymakers, W. Verwaal, E. Meijvogel-de Koning, and L. Douma are thanked for enabling and managing the CT imaging of the cores, and the sample and data exchange.

## ■ ABBREVIATIONS

CT	computed tomography
SEM	scanning electron microscopy
WMF	Whitby Mudstone formation
FEP	fluorinated ethylene propylene
BIB	broad-ion-beam
SE	secondary electron
BSE	backscatter electron

## ■ REFERENCES

- (1) Bossart, P.; Thury, M. Research in the Mont Terri Rock laboratory: Quo vadis? *Phys. Chem. Earth* **2007**, *32*, 19–31.
- (2) Neerdael, B.; Boyazis, J. P. The Belgium underground research facility: Status on the demonstration issues for radioactive waste disposal in clay. *Nucl. Eng. Des.* **1997**, *176*, 89–96.
- (3) Tao, Z.; Clarens, A. Estimating the Carbon Sequestration Capacity of Shale Formations Using Methane Production Rates. *Environ. Sci. Technol.* **2013**, *47*, 11318–11325.
- (4) Marschall, P.; Horseman, S.; Gimmi, T. Characterisation of Gas Transport Properties of the Opalinus Clay, a Potential Host Rock Formation for Radioactive Waste Disposal. *Oil Gas Sci. Technol.* **2005**, *60*, 121–139.
- (5) Lewicki, J. L.; Birkholzer, J.; Tsang, C.-F. Natural and industrial analogues for leakage of CO<sub>2</sub> from storage reservoirs: identification of features, events, and processes and lessons learned. *Environ. Geol.* **2007**, *52*, 457–467.
- (6) Dockrill, B.; Shipton, Z. K. Structural controls on leakage of natural CO<sub>2</sub> geologic storage site: Central Utah, U.S.A. *J. Struct. Geol.* **2010**, *32*, 1768–1782.
- (7) Bond, C. E.; Kremer, Y.; Johnson, G.; Hicks, N.; Lister, R.; Jones, D. G.; Haszeldine, R. S.; Saunders, I.; Gilfillan, S. M. V.; Shipton, Z. K.; Pearce, J. The physical characteristics of a CO<sub>2</sub> seeping fault: The implications of fracture permeability for carbon capture and storage integrity. *Int. J. Greenhouse Gas Control* **2017**, *61*, 49–60.
- (8) Passey, Q. R.; Bohacs, K.; Esch, W. L.; Klimentidis, R.; Sinha, S. From Oil-Prone Source Rock to Gas-Producing Shale Reservoir - Geologic and Petrophysical Characterization of Unconventional Shale Gas Reservoirs. *International Oil and Gas Conference and Exhibition in China*; Society of Petroleum Engineers: Beijing, China, 2010.
- (9) Curtis, J. B. Fractured Shale-Gas Systems. *AAPG Bull.* **2002**, *86*, 1921–1938.
- (10) Amann-Hildenbrand, A.; Ghanizadeh, A.; Krooss, B. M. Transport properties of unconventional gas systems. *Mar. Pet. Geol.* **2012**, *31*, 90–99.
- (11) Gale, J. F. W.; Laubach, S. E.; Olson, J. E.; Eichhuble, P.; Fall, A. Natural fractures in shale: A review and new observations. *AAPG Bull.* **2014**, *98*, 2165–2216.

- (12) Carey, J. W.; Lei, Z.; Rougier, E.; Mori, H.; Viswanathan, H. Fracture-permeability behavior of shale. *J. Unconv. Oil Gas Resour.* **2015**, *11*, 27–43.
- (13) Clarkson, C. R.; Haghshenas, B.; Ghanizadeh, A.; Qanbari, F.; Williams-Kovacs, J. D.; Riazi, N.; Debuhr, C.; Deglint, H. J. Nanopores to megafractures: Current challenges and methods for shale gas reservoir and hydraulic fracture characterization. *J. Nat. Gas Sci. Eng.* **2016**, *31*, 612–657.
- (14) Desbois, G.; Urai, J. L.; Kukla, P. A. Morphology of the pore space in claystones evidence from BIB/FIB ion beam sectioning and cryo-SEM observations. *eEarth* **2009**, *4*, 15–22.
- (15) Loucks, R. G.; Reed, R. M.; Ruppel, S. C.; Jarvie, D. M. Morphology, Genesis, and Distribution of Nanometer-Scale Pores in Siliceous Mudstones of the Mississippian Barnett Shale. *J. Sediment. Res.* **2009**, *79*, 848–861.
- (16) Keller, L. M.; Holzer, L.; Wepf, R.; Gasser, P.; Münch, B.; Marschall, P. On the application of focused ion beam nanotomography in characterizing the 3D pore space geometry of Opalinus clay. *Phys. Chem. Earth* **2011**, *36*, 1539–1544.
- (17) Chalmers, G. R.; Bustin, R. M.; Power, I. M. Characterization of gas shale pore systems by porosimetry, pycnometry, surface area, and field emission scanning electron microscopy/transmission electron microscopy image analyses: Examples from the Barnett, Woodford, Haynesville, Marcellus, and Doig units. *AAPG Bull.* **2012**, *96*, 1099–1119.
- (18) Klaver, J.; Desbois, G.; Urai, J. L.; Littke, R. BIB-SEM study of the pore space morphology in early mature Posidonia Shale from the Hils area, Germany. *Int. J. Coal Geol.* **2012**, *103*, 12–25.
- (19) Houben, M. E.; Desbois, G.; Urai, J. L. A comparative study of representative 2D microstructures in Shaly and Sandy facies of Opalinus Clay (Mont Terri, Switzerland) inferred from BIB-SEM and MIP methods. *Mar. Pet. Geol.* **2014**, *49*, 143–161.
- (20) Houben, M. E.; Barnhoorn, A.; Lie-A-Fat, J.; Ravestein, T.; Peach, C. J.; Drury, M. R. Microstructural characteristics of the Whitby Mudstone Formation (UK). *Mar. Pet. Geol.* **2016**, *70*, 185–200.
- (21) Hemes, S.; Desbois, G.; Urai, J. L.; De Craen, M.; Honty, M. Variations in the morphology of porosity in the Boom Clay Formation: insights from 2D high resolution BIB-SEM imaging and Mercury injection Porosimetry. *Neth. J. Geosci./Geol. Mijnbouw* **2014**, *92*, 275–300.
- (22) Dewhurst, D. N.; Aplin, A. C.; Sarda, J.-P. Influence of clay fraction on pore-scale properties and hydraulic conductivity of experimentally compacted mudstones. *J. Geophys. Res.* **1999**, *104*, 29261–29274.
- (23) Fisher, Q. J.; Knipe, R. J. The permeability of faults within siliciclastic petroleum reservoirs of the North Sea and Norwegian Continental Shelf. *Mar. Pet. Geol.* **2001**, *18*, 1063–1081.
- (24) Ingram, G. M.; Urai, J. L. Top-seal leakage through faults and fractures: the role of mudrock properties. In *Muds and Mudstones: Physical and Fluid Flow Properties*; Aplin, A. C., Fleet, A. J., Macquaker, J. H. S., Eds.; Geological Society, London, Special Publications, 1999; Vol. 158, pp 125–135.
- (25) Caine, J. S.; Evans, J. P.; Forster, C. B. Fault zone architecture and permeability structure. *Geology* **1996**, *24*, 1025–1028.
- (26) Chester, J. S.; Chester, F. M.; Kronenberg, A. K. Fracture surface energy of the Punchbowl fault, San Andreas system. *Nature* **2005**, *437*, 133.
- (27) Faulkner, D. R.; Jackson, C. A. L.; Lunn, R. J.; Schlische, R. W.; Shipton, Z. K.; Wibberley, C. A. J.; Withjack, M. O. A review of recent developments concerning the structure, mechanics and fluid flow properties of fault zones. *J. Struct. Geol.* **2010**, *32*, 1557–1575.
- (28) Mitchell, T. M.; Faulkner, D. R. Towards quantifying the matrix permeability of fault damage zones in low porosity rocks. *Earth Planet. Sci. Lett.* **2012**, *339–340*, 24–31.
- (29) Hobbs, P. R. N.; Entwisle, D. C.; Northmore, K. J.; Sumbler, M. G.; Jones, L. D.; Kemp, S.; Self, S.; Barron, M.; Meakin, J. L. *Engineering Geology of British Rocks and Soils*; Lias Group, British Geological Survey, 2012, Internal Report, OR/12/032, p 323.
- (30) Knipe, R. J.; Jones, G.; Fisher, Q. J. Faulting, fault sealing and fluid flow in hydrocarbon reservoirs: an introduction. In *Faulting, Fault Sealing and Fluid Flow in Hydrocarbon Reservoirs*; Jones, G., Fisher, Q. J., Knipe, R. J., Eds.; Geological Society: London, Special Publications, 1998; Vol. 147, pp vii–xxi.
- (31) Amann, F.; Button, E. A.; Evans, K. F.; Gischig, V. S.; Blümel, M. Experimental study of the brittle behavior of clay shale in rapid unconfined compression. *Rock Mech. Rock Eng.* **2011**, *44*, 415–430.
- (32) Herber, R.; de Jager, J. Geoperspective Oil and Gas in the Netherlands – Is there a future? *Neth. J. Geosci./Geol. Mijnbouw* **2014**, *89*, 91–107.
- (33) Houben, M. E.; Hardebol, N. J.; Barnhoorn, A.; Boersma, Q. D.; Carone, A.; Liu, Y.; de Winter, D. A. M.; Peach, C. J.; Drury, M. R. Fluid flow from matrix to fractures in Early Jurassic shales. *Int. J. Coal Geol.* **2017**, *175*, 26–39.
- (34) Houben, M. E.; Barnhoorn, A.; Wasch, L.; Trabuco-Alexandre, J.; Peach, C. J.; Drury, M. R. Microstructures of Early Jurassic (Toarcian) shales of Northern Europe. *Int. J. Coal Geol.* **2016**, *165*, 76–89.
- (35) Powell, J. H. Jurassic sedimentation in the Cleveland Basin: a review. *Proc. Yorks. Geol. Soc.* **2010**, *58*, 21–72.
- (36) Hangx, S. J. T.; Spiers, C. J.; Peach, C. J. The effect of deformation on permeability development in anhydrite and implications for caprock integrity during geological storage of CO<sub>2</sub>. *Geofluids* **2010**, *10*, 369–387.
- (37) Sutherland, H. J.; Cave, S. P. Argon gas permeability of New Mexico rock salt under hydrostatic compression. *Int. J. Rock Mech. Min. Sci. Geomech. Abstr.* **1980**, *17*, 281–288.
- (38) Peach, C. J.; Spiers, C. J. Influence of crystal plastic deformation on dilatancy and permeability development in synthetic salt rock. *Tectonophysics* **1996**, *256*, 101–128.
- (39) Busch, A.; Bertier, P.; Gensterblum, Y.; Rother, G.; Spiers, C. J.; Zhang, M.; Wentinck, H. M. On sorption and swelling of CO<sub>2</sub> in clays. *Geomech. Geophys. Geo-energ. Geo-resour.* **2016**, *2*, 111–130.
- (40) de Jong, S. M.; Spiers, C. J.; Busch, A. Development of swelling strain in smectite clays through exposure to carbon dioxide. *Int. J. Greenhouse Gas Control* **2014**, *24*, 149–161.
- (41) Zhang, M.; de Jong, S. M.; Spiers, C. J.; Busch, A.; Wentinck, H. M. Swelling stress development in confined smectite clays through exposure to CO<sub>2</sub>. *Int. J. Greenhouse Gas Control* **2018**, *74*, 49–61.
- (42) Houben, M. E.; Barnhoorn, A.; Peach, C. J.; Drury, M. R. Potential permeability enhancement in Early Jurassic shales due to their swelling and shrinkage behavior. *Int. J. Coal Geol.* **2018**, *196*, 115–125.
- (43) Peach, C. J.; Spiers, C. J. Influence of crystal plastic deformation on dilatancy and permeability development in synthetic salt rock. *Tectonophysics* **1996**, *256*, 101–128.
- (44) Viggiani, G.; Lenoir, N.; Bésuelle, P.; Dimichiel, M.; Marello, S.; Desrues, J.; Kretschmer, M. X-ray microtomography for studying localized deformation in fine-grained geomaterials under triaxial compression. *C. R. Mécanique* **2004**, *332*, 819–826.
- (45) Bésuelle, P.; Viggiani, G.; Lenoir, N.; Desrues, J.; Bornert, M. X-ray Micro CT for studying Strain Localization in Clay Rocks under Triaxial Compression. *Advances in X-ray Tomography for Geomaterials*; John Wiley & Sons, 2006.
- (46) Carey, J. W.; Rougier, E.; Lei, Z.; Viswanathan, H. *Experimental Investigation of Fracturing of Shale with Water*; American Rock Mechanics Association, 2015; Vol. 15, p 389.
- (47) Frash, L. P.; Carey, J. W.; Lei, Z.; Rougier, E.; Ickes, T.; Viswanathan, H. S. High-stress triaxial direct-shear fracturing of Utica shale and in situ X-ray microtomography with permeability measurement. *J. Geophys. Res.: Solid Earth* **2016**, *121*, 5493.
- (48) Hemes, S.; Desbois, G.; Urai, J. L.; Schröppel, B.; Schwarz, J.-O. Multi-scale characterization of porosity in Boom Clay (HADES-level, Mol, Belgium) using a combination of X-ray  $\mu$ -CT, 2D BIB-SEM and FIB-SEM tomography. *Microporous Mesoporous Mater.* **2015**, *208*, 1–20.

(49) Voorn, M.; Exner, U.; Barnhoorn, A.; Baud, P.; Reuschlé, T. Porosity, permeability and 3D fracture network characterisation of dolomite reservoir rock samples. *J. Pet. Sci. Eng.* **2015**, *127*, 270.

(50) Caine, J. S.; Evans, J. P.; Forster, C. B. Fault zone architecture and permeability structure. *Geology* **1996**, *24*, 1025–1028.

(51) Shipton, Z. K.; Cowie, P. A. Damage zone and slip-surface evolution over  $\mu\text{m}$  to km scales in high-porosity Navajo sandstone, Utah. *J. Struct. Geol.* **2001**, *23*, 1825–1844.

(52) McBeck, J.; Kobchenko, M.; Hall, S. A.; Tudisco, E.; Cordonnier, B.; Meakin, P.; Renard, F. Investigating the Onset of Strain Localization Within Anisotropic Shale Using Digital Volume Correlation of Time-Resolved X-Ray Microtomography Images. *J. Geophys. Res.* **2018**, *123*, 7509.

(53) Fink, R.; Krooss, B. M.; Gensterblum, Y.; Amann-Hildenbrand, A. Apparent permeability of gas shales – superposition of fluid-dynamic and poro-elastic effects. *Fuel* **2017**, *199*, 532–550.

(54) McKernan, R.; Mecklenburgh, J.; Rutter, E.; Taylor, K. Microstructural controls on the pressure-dependent permeability of Whitby mudstone. In *Geomechanical and Petrophysical Properties of Mudrocks*; Rutter, E. H., Mecklenburgh, J., Taylor, K. G., Eds.; Geological Society, London, Special publications, 2017; p 454.

(55) Sone, H.; Zoback, M. D. Time-dependent deformation of shale gas reservoir rocks and its long-term effect on the in-situ state of stress. *Int. J. Rock Mech. Min. Sci.* **2014**, *69*, 120–132.

(56) Bourg, I. C. Sealing shales versus brittle shales: A sharp threshold in the material properties and energy technology uses of fine-grained sedimentary rocks. *Environ. Sci. Technol. Lett.* **2015**, *2*, 255–259.

(57) Douma, L. A. N. R.; Primarini, M. I. W.; Houben, M. E.; Barnhoorn, A. The validity of generic trends on multiple scales in rock-physical and rock-mechanical properties of the Whitby Mudstone, United Kingdom. *Mar. Pet. Geol.* **2017**, *84*, 135–147.

(58) Zhubayev, A.; Houben, M. E.; Smeulders, D. M. J.; Barnhoorn, A. Ultrasonic velocity and attenuation anisotropy of shales (Whitby, UK). *Geophysics* **2016**, *81*, D45–D56.

(59) Sone, H.; Zoback, M. D. Mechanical properties of shale-gas reservoir rocks – Part I: Static and dynamic elastic properties and anisotropy. *Geophysics* **2013**, *78*, D381–D392.

(60) Bossart, P.; Meier, P. M.; Moeri, A.; Trick, T.; Mayor, J.-C. Geological and hydraulic characterization of the excavation disturbed zone in the Opalinus Clay of the Mont Terri Rock Laboratory. *Eng. Geol.* **2002**, *66*, 19–38.

(61) Zhang, M. Stress-strain-sorption behaviour and permeability evolution in clay-rich rocks under CO<sub>2</sub> storage conditions. *Utrecht Studies in Earth Sciences* **2019**, *188*, 217.

(62) Douma, L. A. N. R.; Dautriat, J.; Sarout, J.; Dewhurst, D. N.; Barnhoorn, A. Impact of water saturation on the elastic anisotropy of the Whitby Mudstone, United Kingdom. *Geophysics* **2020**, *85*, MR57–MR72.

(63) Snow, D. T. Rock Fracture Spacings, Openings, and Porosities. *J. Soil Mech. Found. Div.* **1968**, *94*, 73–91.

(64) Witherspoon, P. A.; Wang, J. S. Y.; Iwai, K.; Gale, J. E. Validity of Cubic Law for Fluid Flow in a Deformable Rock Fracture. *Water Resour. Res.* **1980**, *16*, 1016–1024.

(65) Van Stappen, J. F.; Meftah, R.; Boone, M. A.; Bultreys, T.; De Kock, T.; Blykers, B. K.; Senger, K.; Olausson, S.; Cnudde, V. In Situ triaxial testing to determine fracture permeability and aperture distribution for CO<sub>2</sub> sequestration in Svalbard, Norway. *Environ. Sci. Technol.* **2018**, *52*, 4546–4554.

(66) Hakami, E.; Larsson, E. Aperture Measurements and Flow Experiments on a Single Natural Fracture. *Int. J. Rock Mech. Min. Sci. Geomech. Abstr.* **1996**, *33*, 395–404.

(67) Nick, H. M.; Paluszny, A.; Blunt, M. J.; Matthai, S. K. Role of Geomechanically Grown Fractures on Dispersive Transport in Heterogeneous Geological Formations. *Phys. Rev. E: Stat., Nonlinear, Soft Matter Phys.* **2011**, *84*, 056301.